Hot-Electron Energy Coupling in Ultraintense Laser-Matter Interaction

A. J. Kemp,[1] Y. Sentoku,[2] and M. Tabak[1]
[1]Lawrence Livermore National Laboratory, Livermore, California 94551, USA
[2]University of Nevada, Reno, Nevada 89577, USA
(Received 28 April 2008; published 14 August 2008)

We investigate the hydrodynamic response of plasma gradients during the interaction with ultraintense energetic laser pulses, using kinetic particle simulations. Energetic laser pulses are capable of compressing preformed plasma gradients over short times while accelerating low-density plasma backwards. As light is absorbed on a steepened interface, hot-electron temperature and coupling efficiency drop below the ponderomotive scaling, and we are left with a new absorption mechanism that strongly relies on the electrostatic potential caused by low-density preformed plasma. We describe this process, explain electron spectra, and identify the parameter regime where strong compression occurs. Finally, we discuss the implications for fast ignition and other applications.

DOI: 10.1103/PhysRevLett.101.075004 PACS numbers: 52.38.−r, 52.50.Jm, 52.65.Rr

While intense short laser pulses offer many interesting applications for high-energy density physics [1], coupling and transport of energy into dense plasma in the ultrarelativistic intensity regime are poorly understood due to the complex dynamics near the absorption point and difficult to model due to the several orders of magnitude between the dense-plasma response time and corresponding length and the scales of the laser spot size and pulse duration. An additional problem is the large-scale, low-density blowoff plasma in front of the actual solid target found in high-energy short-pulse experiments. It is created before the arrival of the main pulse by amplified spontaneous emission processes in the laser that cannot be easily suppressed and is dense enough as to prevent light propagation several micrometers away from the target. For a recent high-energy short-pulse experiment, scale lengths of about $l_s = 0.5$–$1.0\ \mu$m between the solid and a fraction of critical density $n_c = 1.1 \times 10^{21}\ \mathrm{cm}^{-3}$ were found, preceded by a longer scale length plasma [2]. For fast-ignition experiments, one expects $l_s \leq 10\ \mu$m, depending on the energy in the prepulse.

This Letter addresses the short-pulse laser-driven dynamics of preformed plasma in the limit of ultraintense, energetic pulses over a picosecond. At intensities $I_L = 1.37 \times 10^{20}\ \mathrm{W/cm^2}$, the vacuum energy density of light corresponds to ≥ 30 G bar at 1 μm wavelength light. Such a pressure can cause ions to move over several microns in less than 1 ps. Many early works on absorption consider idealized step function density profiles, relatively short density gradients, or large volumes [3,4], effectively neglecting the large-scale ion motion. We characterize the response of plasma gradients in the limit of normal incidence with one spatial and three velocity degrees of freedom in a fully relativistic kinetic description. Our approach allows us to isolate a 1D "hydrodynamic"—from purely multidimensional effects, such as beam filamentation [5], hole boring [6], and deformations of the plasma surface through Rayleigh-Taylor-like instabilities [7]. We ignore refluxing of hot electrons, which can occur due to electrostatic confinement in thin foils.

We first consider two plasma density gradients with different scale lengths. Standard particle-in-cell (PIC) simulations [8] show how the laser-generated pressure near the relativistic critical density causes a strong compression of the preplasma towards higher densities and acceleration into vacuum of plasma at lower densities, followed by a drop in absorption and hot-electron temperature. Subsequent model simulations with fixed ions help to understand this. We find key properties of the laser-generated electron distribution at ultrarelativistic intensities; expressions for cutoff energies and temperatures are given. Combined with an analytical description of the compression, which depends on plasma scale length, ion charge-to-mass ratio, and laser intensity, wavelength, and pulse duration, this is useful for defining plasma parameters at which absorption remains high over the laser pulse duration, and the electron temperature is within the parameter band for fast ignition (FI) or other applications [1]. Simulations were performed with the kinetic PIC code LPIC [9] using a resolution of 500–1000 cells per laser wavelength and up to 300 particles per species and cell, thus resolving the plasma's Debye length at the highest density and initial temperature of 10 keV, and verified with an up to 3× higher resolution.

Figure 1 depicts the evolution of an initially exponential plasma profile during the interaction with an ultraintense laser pulse. Shown is a contour plot of ion density versus space and time for a gradient scale length of 0.85 μm, beginning at time 70τ, where $\tau \equiv \lambda/c \approx 3.3$ fs is the laser period and $n_c = \pi m_e c^2/(e\lambda)^2$ is the critical density. Between 90 and 100 μm, the density profile is uniform, representing a solid target region. Plasma ions have a mass $M_i = 8m_p$, where m_p is the proton mass and charge state $Z = 1$. Light enters the box at $x = 0$ with an intensity of $1.37 \times 10^{20}\ \mathrm{W/cm^2}$ at $\lambda = 1\ \mu$m and a semi-infinite pulse envelope. The vacuum region between the left box

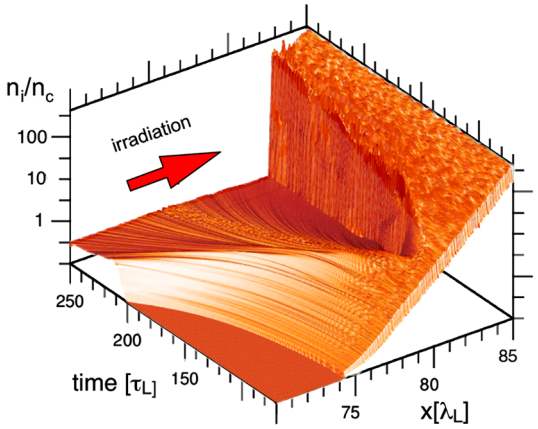

FIG. 1 (color online). Deformation of an exponential density gradient with scale length $l_s = 0.85\ \mu$m and peak density $n_{i,\max} = 400 n_c$, irradiated by a laser pulse with intensity $I_L = 1.37 \times 10^{20}$ W/cm^2, wavelength/period $\lambda = 1\ \mu$m, $\tau = 3.3$ fs.

boundary and the plasma gradient allows for a free expansion over the simulation time of $350\tau_L$.

Figure 2 gives details of this "short gradient" (SG) case shown in Fig. 1 and a "long gradient" (LG) case with a scale length of 3.25 μm. Shown are snapshots of ion density, as well as corresponding electron spectra and fast electron energy flux density recorded in the solid density region $W_{e,x} = \sum_{x=x_d} n_e(\gamma - 1)v_x$, averaged over a laser cycle and normalized to the average laser energy flux $\langle W_L \rangle = I_L/2$. We have checked that the energy flux and spectra are independent of where exactly in the solid target region they are recorded. Additionally, the spectra of

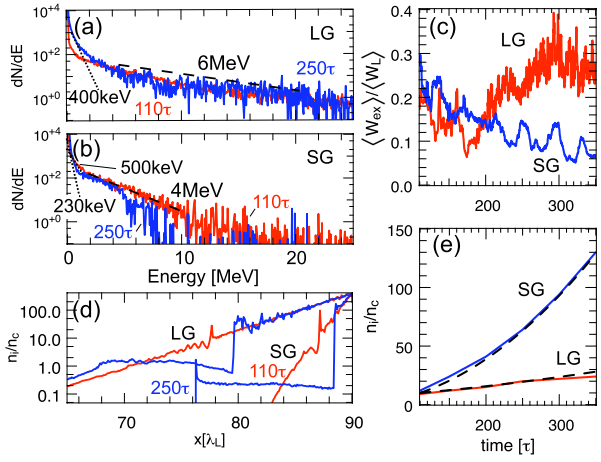

FIG. 2 (color online). Absorption and electron transport in exponential density gradients at $I_L = 1.37 \times 10^{20}$ W/cm^2. (a) Electron spectra at two times for a LG case with $l_s = 3.25\ \mu$m; (b) for a SG with $l_s = 0.85\ \mu$m; (c) average electron energy flux density $\langle W_{ex} \rangle$, normalized to the laser intensity W_L for SG and LG, recorded behind the density gradient at $x_d = 95\ \mu$m; (d) snapshots of ion density at $t = 110$ and 250τ; (e) front density vs analytical result (dashed line).

all electrons passing through a single cell over a 10τ time interval give nearly identical results. Figures 2(a) and 2(b) show electron spectra for the LG and SG cases at two times, illustrating how they evolve from initially similar characteristics in temperature and number to quite different regimes at a later time, when hydrodynamics has changed the shape of the gradient. The LG spectrum maintains its high-energy tail at ~6 MeV consistent with the ponderomotive scaling [7]. Note that more than 2/3 of the total energy contained in the LG spectrum is at energies below 5 MeV. In the late SG spectrum, high-energy particles have almost disappeared. Also, the average energy of the low-energy hot-electron population (slope temperature <1 MeV at 250 fs) in SG is smaller than in LG by the square root of the density ratio at the steepened interface; compare Fig. 2(e) [10]. Figure 2(c) gives the time dependence of the electron energy flux $\langle W_{ex} \rangle / \langle W_L \rangle$ in both cases. Figure 2(d) shows corresponding ion density profiles at two times. In both cases, coupling of the intense laser pulse drives an electrostatic shock wave towards the solid at a speed of $\approx 0.01c$ [11–13], while it accelerates plasma backwards forming a flat "lower shelf." Two remarkable differences between these two cases are (a) a 4× higher density of the lower-shelf plasma at 250τ in the LG case and (b) its 4× lower density at the location of the shock. These lead to differences in absorption discussed below. Also note the shoulderlike electron energy spectrum at 250τ in the SG case, which will be discussed below. Additional simulations at a hundred times reduced laser intensity show a much lesser impact on the plasma profile, leading to a nearly constant absorption of roughly 30%.

The compression of the plasma gradient shown in Fig. 2(e) can be described using momentum conservation at the front, i.e., where light is reflected [6,7],

$$(1 + R) I_L / c = 2 M_i u_f^2 n_i \qquad (1)$$

in a frame moving at velocity u_f with the front. Here $R \approx 1$ is a good approximation of the 1D plasma reflectivity, and n_i is the ion density, neglecting electron momentum. This is valid only in the ultrarelativistic case [6]. Reflection and profile steepening occur at the relativistic critical density $\gamma_{os} n_c$, with $\gamma_{os} = \sqrt{1 + (1 + R) a_0^2/2}$ [4,6]; compare Fig. 2(d). Below this density, electrons are accelerated to relativistic Maxwellian distributions with average energy $m_e c^2 (\gamma_{os} - 1)$ [7], consistent with Figs. 2(a) and 2(b). The time-dependent compression of a profile $n_i(x) = (\gamma_{os} n_c / Z) \exp[(x - x_c)/l_s]$ with scale length l_s is obtained by solving Eq. (1) for u_f and integrating

$$x_f(t) = x_c + 2 l_s \ln\left[1 + t \frac{c}{2 l_s} \left(\frac{m_e Z}{2 M_i} \frac{\gamma_{os}^2 - 1}{\gamma_{os}}\right)^{1/2}\right] \qquad (2)$$

to find the location of the front. Equation (2) is written in terms of γ_{os} using $I_L/c = m_e c^2 n_c a_0^2/2$ for $\lambda = 1\ \mu$m. Figure 2(e) plots the corresponding interface density at the

front vs time and simulation results. Expansion of the plasma towards vacuum is characterized by the fact that the outward accelerated mass is nearly constant and by $v_i \propto (x - x_c)(t - t_0)$, forming a density plateau. The ion bump at the front of the expansion has been discussed earlier [14].

In order to understand the evolution of absorption and electron flux in the density gradients above, we now turn to a "quasistatic" scenario in which the ion motion is suppressed. Instead of an exponential ramp, we use a 3 μm layer of lower-shelf plasma at uniform ion density n_s in front of a 10 μm layer of plasma at "solid" density $200n_c$ (in most cases). Figure 3 shows the electron spectra and the electrostatic field near the boundary for several densities n_s, as well as cycle-averaged electron energy flux $\langle W_{\rm ex}\rangle/\langle W_L\rangle$. Locations of the lower shelf and a small part of the bulk plasma are indicated by a shaded area in Fig. 3(b).

Depending on the density-length product of the lower shelf, electrons are pushed into the bulk by the ponderomotive pressure. The maximum arial charge that can be pushed into the bulk is determined by a balance between the laser and electrostatic field energy

$$2I_L/c = en_s\phi_s, \tag{3}$$

with $\phi_s = 2\pi e n_s l_s^2$, assuming no absorption. Normalization yields $a_L^2 = 2\pi^2(n_s/n_c)^2(l_s/\lambda)^2$. For $a_L = 10$ and $l_s = 3$ μm, we find $n_{s,0} = 0.75n_c$ for the critical, i.e.,

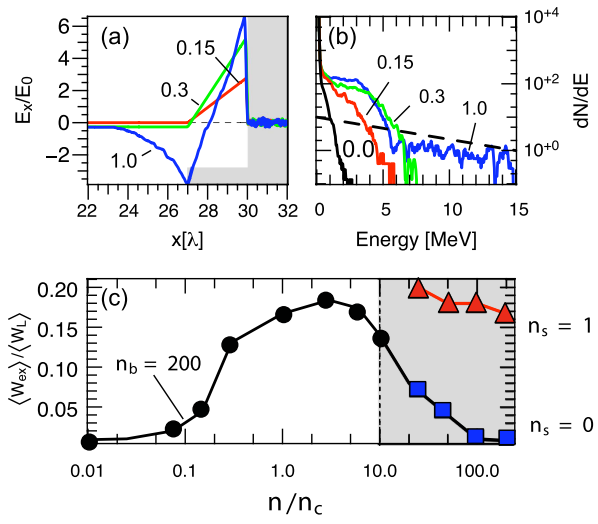

FIG. 3 (color online). Absorption and electron transport in step function density profiles at $I_L = 1.37 \times 10^{20}$ W/cm^2. (a) Electron spectra for various values of the shelf density parameter n_s as indicated. The dashed line gives a 6.7 MeV slope consistent with Ref. [7]; (b) corresponding snapshots of E_x; location of shelf and bulk target are indicated by the shaded area; (c) laser-to-electron coupling efficiency vs plasma density. For $n_s \leq 10$, targets consist of a 3 μm long lower shelf at density n_s followed by 10 μm of plasma at $200n_c$; for $n_s \geq 10$, plasma is uniform. Rectangular symbols refer to $n_s = 0$ and triangles to $n_s = 1$.

maximum, density that can be pushed into the bulk. On the other hand, by fixing $n_s = n_c$ we get a maximum shelf length of 2.25 μm, consistent with Fig. 3(b), where $E_0 = m_e\omega c/e$. The maximum electric field at the interface $E_{x,i}^{\rm max} = a_0/\sqrt{2}$ is reached when the shelf arial density $n_s l_s$ of Eq. (3) is critical, which also agrees with Fig. 3 (b) after accounting for some absorption; see Fig. 3(c). As the electric field at the interface increases with n_s, the electron spectrum extends to higher maximum energies and forms a shoulderlike distribution. When the lower-shelf density exceeds the critical value (here $n_s \geq 1$), hot electrons that remain in the shelf cause an ambipolar electrostatic field, and an additional tail in the distribution function appears [7] that is absent for smaller values of n_s.

Key features of the spectra are reproduced by a simple model of electron acceleration near the interface, under the condition that the lower shelf is just critical. The laser electric and magnetic fields in vacuum near an almost perfectly reflective boundary at $x = 0$ with density n_p are given by [15] $E_y = 2a_0 \sin(2\pi x + \phi)\cos(2\pi t)$ and $B_z = 2a_0 \cos(2\pi x + \phi)\sin(2\pi t)$, respectively, where $\tan(\phi) = -\sqrt{n_c/n_p}$. An electron at $(x, t) = (0, 0)$ is extracted by the longitudinal electric field $E_{x,i}$ into the region where the laser electric field reaches its peak value. In this process the electron gains negative (mostly) transverse momentum until the longitudinal component of the Lorentz force exceeds E_x. The "extraction" time t' can be found by integrating the equation of motion $\partial p_x/\partial t = -2\pi E_{x,i} + 4\pi a_0 \sin(2\pi t)$, assuming that $v_y \approx -1$ with normalized momenta p and velocities $v = p/\sqrt{1 + |p|^2}$. Solving for $p_x(t') = 0$ in the case of a critical plasma shelf, we find $t' \approx 0.12$. After this time, no further particles can be extracted. Electrons at $x' = -t'$ are now accelerated by the Lorentz force towards the boundary over a similar time interval, so that they gain a longitudinal momentum not larger than $p_x^{\rm max} = 4\pi a_0 t' \approx 1.45a_0$. For $a_0 = 10$, this expression predicts a cutoff energy $E_{\rm max} \approx 7$ MeV, in agreement with Fig. 3(a) (curve labeled "0.3"). The shoulderlike feature of the spectrum stems from (i) electrostatic shielding of electrons extracted during the time interval $[0, t']$ by the charges of other electrons and (ii) their relative phase with respect to the electromagnetic field pattern. For larger amounts of lower-shelf plasma, the "shoulder" remains unchanged, and an additional tail of hot electrons appears that originates in the low-density plasma where both light and plasma are present [7]. For an undercritical lower shelf, where E_x is determined by the arial charge $n_s l_s$, the spectrum is independent of intensity, because $t' \propto E_{x,i}/a_0$ while $p_x^{\rm max} \propto a_0 t'$. We have verified this by simulations at different laser amplitudes, not shown here. Without the lower-shelf plasma, there is no electrostatic extraction of electrons, so acceleration occurs in the evanescent mode of E_y, giving a much smaller absorption scaling with density as $1/\sqrt{n}$ [10]. The extraction or ac-

celeration process repeats itself at time $\tau/2$ with $p_y > 0$, leading to the well-known $2\omega_0$ electron jets [3]. Figure 3(c) plots time-averaged electron flux (absorption) vs plasma density in a combination of two separate scenarios: At low density $n/n_c < 10$, density refers to a 3 μm thick lower shelf preceding a 10 μm layer of bulk plasma at a constant density of $200n_c$; compare Fig. 3(a). Light propagates through the lower-shelf plasma because it is relativistically undercritical [4]. For higher densities $n/n_c \geq 10$, the plasma becomes opaque. Here the quantity n refers to the density of a 10 μm thick uniform plasma layer; both scenarios give the same result for $10n_c$. The effect of changing the bulk plasma density while keeping $n_s = 0.1n_c$ is small, as shown in a separate curve. Comparison of this curve for $n_s = 1$ (triangles) with the $n_s = 0$ curve (rectangles) demonstrates that (i) absorption depends critically on the preplasma, (ii) it is nearly independent of bulk density with $n_s \geq 1$, and (iii) it drops slightly with bulk density when $n_s \ll 1$. This is representative of the decrease in absorption seen in Fig. 2, where the lower-shelf density drops due to the hot-electron pressure, while the interface is compressed over time. In one spatial dimension, this effect can be slowed down only by choosing longer gradient lengths for the preformed plasma, i.e., more energy in the prepulse, or lower intensities.

A fiducial simulation of a step function density profile with mobile ions at a density $100n_c$ and an intensity $I_L = 10^{18}$ W/cm^2 yields an absorption fraction of 14% for an initial electron temperature of 10 keV, which agrees well with results published earlier [3]. This relatively high value is caused by thermal expansion of the bulk plasma and the subsequent formation of a density gradient similar to the ones discussed above. However, in runs with initially cold electrons, i.e., <1 keV, or at intensities around 10^{20} W/m^2, the expansion is suppressed by the ponderomotive pressure and absorption drops to $<1\%$. We find that the initial electron temperature is much less relevant at ultrahigh laser intensity, mainly because the electron momentum in the laser field greatly exceeds their initial thermal momentum.

While collisions play no direct role for absorption in plasma density gradients around 10–$30n_c$ and keV temperatures, they could contribute indirectly by causing strong electrostatic fields in resistive dense plasma. This could cause the refluxing of hot electrons even in large FI-relevant targets and enhance absorption and electron temperature. Results are scalable with respect to laser wavelength using the relation $I\lambda^2 \propto a_0^2$; i.e., for a given intensity, a smaller wavelength leads to smaller a_0. Under oblique incidence, absorption tends to be much higher than under normal incidence because the laser electric field has a $<90°$ angle to the target surface [16,17]. This will affect the momentum balance Eq. (2). However, for small angles α, both Poynting flux and critical density are reduced by a factor $\cos^2\alpha$, so that we do not expect drastic changes. Backscattering of the ultraintense light in underdense plasma is found to be only a minor effect. Current filamentation in low-density plasma will alter absorption for large-scale lengths $l_s > 1$ μm, but for the short gradient case presented in Fig. 1 we expect hydrodynamic effects to dominate, depending on laser spot size, etc.

In conclusion, preformed plasma is beneficial for high absorption at MeV electron energies in ultrahigh intensity short-pulse laser experiments. At intensities around 10^{20} W/cm^2, the ponderomotive pressure, exerted via an ambipolar electrostatic field around the point of absorption, compresses plasma at greater-than-critical density leading to a steepening of the interface. At the same time, it accelerates low-density plasma away from the interaction region and thereby reduces absorption over a time scale determined by the plasma gradient length and laser parameters, typically subpicosecond. Recent simulations or experiments at such intensities have demonstrated that compression of preformed plasma can lead to laser-driven shock waves [13], as well as dominant coupling into a sub-MeV electron population [10]. The latter result indicates that 2D effects will give higher and less density-dependent absorption than seen in 1D. In combination with the mechanism discussed here, this means that it is possible to efficiently generate soft electron spectra useful for fast ignition.

A. J. K. acknowledges stimulating discussions with M. Key, W. Kruer, H. Ruhl, and S. Wilks. This work was performed under the auspices of the U.S. Department of Energy by LLNL under Contract No. DE-AC52-07NA27344 and under Cooperative Agreement No. DE-FC02-04ER54789.

[1] M. Tabak *et al.*, Phys. Plasmas **1**, 1626 (1994).
[2] W. Theobald *et al.*, Phys. Plasmas **13**, 043102 (2006).
[3] W. Kruer and K. Estabrook, Phys. Fluids **28**, 430 (1985).
[4] E. Lefebvre *et al.*, Phys. Rev. Lett. **74**, 2002 (1995).
[5] A. Pukhov *et al.*, Phys. Rev. Lett. **76**, 3975 (1996).
[6] Y. Sentoku *et al.*, Fusion Sci. Technol. **49**, 278 (2006).
[7] S. Wilks *et al.*, Phys. Rev. Lett. **69**, 1383 (1992).
[8] C. K. Birdsall and A. B. Langdon, *Plasma Physics via Computer Simulation* (Adam Hilger, New York, 1991).
[9] R. Pfund *et al.*, in *Superstrong Fields in Plasmas*, edited by M. Lontano *et al.*, AIP Conf. Proc. No. 426 (AIP, New York, 1998), p. 141.
[10] B. Chrisman *et al.*, Phys. Plasmas **15**, 056309 (2008).
[11] L. Silva *et al.*, Phys. Rev. Lett. **92**, 015002 (2004).
[12] J. Denavit, Phys. Rev. Lett. **69**, 3052 (1992).
[13] K. Akli *et al.*, Phys. Rev. Lett. **100**, 165002 (2008).
[14] A. V. Gurevich *et al.*, Sov. Phys. JETP **53**, 937 (1981).
[15] M. Born and E. Wolf, *Principles of Optics* (Pergamon, New York, 1975).
[16] F. Brunel, Phys. Rev. Lett. **59**, 52 (1987).
[17] P. Gibbon and A. Bell, Phys. Rev. Lett. **68**, 1535 (1992).